



# Improved lithium storage performance of block-like Sn/SnO<sub>2</sub> powders wrapped in the hydrogel-derived carbon layer as composite anode materials

Weiguo Zheng<sup>1,2,3</sup> · Shuqing Nie<sup>1,3</sup> · Kaiyi Chen<sup>2</sup> · Rui Li<sup>2,3</sup> · Yao Qin<sup>1,2</sup> · Wei Xiao<sup>3</sup>

Received: 26 April 2022 / Revised: 14 June 2022 / Accepted: 20 July 2022 / Published online: 28 July 2022  
© The Author(s), under exclusive licence to Springer-Verlag GmbH Germany, part of Springer Nature 2022

## Abstract

Novel nitrogen-doped carbon (NC) coating encapsulating block-like Sn/SnO<sub>2</sub> (Sn/SnO<sub>2</sub>@NC) composite powders are successfully synthesized via hydrothermal, sol-gel, and subsequent heat treatment processes, which are characterized by XRD, SEM, thermogravimetric, Raman, and XPS. The results indicate that the Sn/SnO<sub>2</sub>@NC-2 composite powders are uniformly distributed in the NC matrix in the presence of 7.000 g of acrylamide. Moreover, the Sn/SnO<sub>2</sub>@NC-2 composite powders deliver high initial discharge specific capacity of 1132 mAh g<sup>-1</sup> and decent capacity of 471.4 mAh g<sup>-1</sup> after 100 cycles at 100 mA g<sup>-1</sup> when the composite powders are evaluated as anode materials for lithium-ion batteries. The improved electrochemical performance of Sn/SnO<sub>2</sub>@NC-2 is mainly ascribed to the NC coating that can relieve the volume expansion and provide multiple charge transfer channels for electrons to consolidate the structural stability and promote the electronic conductivity of the Sn/SnO<sub>2</sub> anode materials, respectively. Therefore, the Sn/SnO<sub>2</sub>@NC-2 composite powders can be a promising and attractive anode material for lithium-ion batteries.

**Keywords** Nitrogen-doped carbon · Sn/SnO<sub>2</sub> · Block-like · Anode · Lithium-ion battery

## Introduction

Developing the high-efficiency energy storage system is vitally important to solve the problems of increasingly scarce energy resources and serious environmental pollution [1–3]. Among various storage energy device, lithium-ion batteries (LIBs) are widely applied in a diverse range of portable electronic equipment and even occupy the prime market in the field of electric vehicles, which are favored by their unique properties, such as high energy/power density, wide working temperature range, low self-discharge rate,

eco-friendliness, and long cycle life [4–6]. With the fast progress of the technology, the performance of LIBs has gained significant improvements [7–9]. Nonetheless, it is still struggling with some intractable technical challenges that the speedy development of those applications is mostly powered by advanced LIBs, which leads to the increasing demands being placed on advanced LIBs according to higher specific capacity, much better rate capabilities and durability [10–12]. Exploring the anode materials is a key method to optimize the specific capacity of the whole battery system [13–15]. However, the limited theoretical capacity of graphite cannot meet the demands even though it possesses good conductivity, high crystallinity, and perfect crystal structure with a spacing of approximately 0.3354 nm that can make lithium ions freely embedded into its interlayer to form Li<sub>x</sub>C<sub>6</sub> (0 ≤ x ≤ 1) intercalation compounds [16–18]. Tin (Sn)-based materials are exploited as substitutes for graphite and considered as one of the most promising anode materials for LIBs, which are associated with their advantages of abundant resources, high theoretical specific capacity, and low discharge potential (< 0.5 V vs. Li/Li<sup>+</sup>) during the alloying/dealloying reaction. Moreover, both metallic tin (994 mAh g<sup>-1</sup>) and tin oxide electrodes (SnO: 875 mAh g<sup>-1</sup>, SnO<sub>2</sub>:

✉ Wei Xiao  
xwylyq2006@126.com

<sup>1</sup> Hunan Provincial Key Laboratory of Water Treatment Functional Materials, College of Chemistry and Materials Engineering, Hunan University of Arts and Science, Changde 415000, People's Republic of China

<sup>2</sup> Sanjin Group Hunan Sanjin Pharmaceutical Co., Changde 415000, People's Republic of China

<sup>3</sup> College of Chemistry and Environmental Engineering, Yangtze University, Jingzhou 434023, People's Republic of China

783 mAh g<sup>-1</sup>) possess high theoretical capacity that is much higher than that of graphite (372 mAh g<sup>-1</sup>) [19–21]. However, the poor rate capacity and cyclability resulted from the pulverization and cracking of the electrodes during the lithiation/delithiation process, thus causing the active particles to detach from the current collector, which hampers further industrial application of the Sn-based materials. To gain high-performance Sn-based anode materials, effective improvements are carried out to tackle the above disadvantages, which include reducing the particle-size to the nanoscale, and constructing a physical buffer layer by introducing carbon materials such as carbon nanotubes (CNTs), graphene, pyrolytic carbon, and biochar [22–24]. Although the former strategy provides improved cycle stability for a bulk anode, the ultrasmall-sized particles tend to aggregate and then form larger particles in the subsequent cycling processes, leading to severe mechanical degradation problems of the electrode [25–27].

Significantly, the block-like Sn/SnO<sub>2</sub> powders have attracted extensive attention due to the high specific capacity and flexible reaction kinetics. In addition, metallic tin can reversibly react with lithium to form a variety of alloys, in which the maximum intake of lithium atoms reaches 4.4 to form Li<sub>4.4</sub>Sn. Tin oxide generally undergoes a conversion reaction ( $\text{SnO}_2 + 4\text{Li}^+ + 4e^- \leftrightarrow \text{Sn} + 2\text{Li}_2\text{O}$ ) and an alloying reaction ( $\text{Sn} + x\text{Li}^+ + xe^- \leftrightarrow \text{Li}_x\text{Sn}$ ), which can provide suitable conditions for the alloying process and facilitate the splendid cycling behavior [28–30]. At present, two main methods are reported to synthesize the Sn/SnO<sub>2</sub> composite powders, in which one is to mix Sn and SnO<sub>2</sub> directly, and the other is to partially reduce SnO<sub>2</sub> by the thermal reduction [31]. However, most of the products prepared by these methods present poor electrochemical properties or require high technical conditions [32–34]. In our previous work, we have proposed SnO microcube anode materials and synthesized Sn/SnO<sub>2</sub> composite powders with the heterogeneous structure according to the properties of SnO that can be easily converted into Sn and SnO<sub>2</sub> in the inert gas at an appropriate temperature [35]. It is worth noting that SnO powders, inexpensive, nontoxic, and P-type semiconductor oxide, are viable precursor for the fabrication of Sn/SnO<sub>2</sub> anode materials [36–38]. In addition, coupling nitrogen-doped carbon (NC) with Sn/SnO<sub>2</sub> is highly desirable for achieving improved long-term cycling stability of the Sn/SnO<sub>2</sub> electrode material [39–41]. In this work, we have engineered and prepared the Sn/SnO<sub>2</sub> composite powders coated with NC layer as an anode material, in which the structural instability of the Sn/SnO<sub>2</sub> electrode in the cycling processes can be effectively alleviated by NC coating and the ion/electron transfer rate is largely promoted by the heterogeneous structure. The improvements of the electrochemical properties of the Sn/SnO<sub>2</sub>@NC composite powders are investigated, and the effect of different contents of the NC layer on the

structure and electrochemical properties of Sn/SnO<sub>2</sub>@NC composite electrodes are also studied in detail.

## Experimental

### Synthesis of Sn/SnO<sub>2</sub>@NC

SnO microcubes are prepared according to our previous works, in which 2.240 g of SnSO<sub>4</sub> and 3.00 mL of N<sub>2</sub>H<sub>4</sub>·H<sub>2</sub>O (1 mol L<sup>-1</sup>) as raw materials are first added to 140.00 mL of deionized water with constant stirring. Then, the homogeneous milky solution is transferred into a 200-mL hydrothermal reactor and maintained at 150 °C for 12 h. The collected product is centrifuged and washed several times with deionized water and ethanol to remove the reaction residue. The final product SnO precursor powders are obtained after being dried in a vacuum oven at 80 °C for 12 h.

The targeted Sn/SnO<sub>2</sub>@NC hybrid powders are prepared by first encapsulating SnO microcubes in the hydrogel and then carbonizing the coated composite powders. In the first step, a certain amount of acrylamide and 0.010 g of methylene-bisacrylamide powders are dissolved in 15.00 mL of deionized water in the presence of 5.00 mL of ammonium persulfate solution with a concentration of 1.000 g L<sup>-1</sup> to form a clear and transparent solution with incessant stirring. In the second step, 1.00 mL of the liquid supernatant and 0.210 g of SnO powders are added to a test tube and vigorously ultrasonicated for 15 min to realize uniform dispersion, and the test tube containing the black solution is transferred to a bath at 80 °C and stirred for 15 min. The polymerized samples are pre-oxidized in air at 200 °C for 2 h with a heating rate of 2 °C min<sup>-1</sup>. Subsequently, the samples are carbonized in a nitrogen atmosphere at 600 °C for 2 h with a heating rate of 5 °C min<sup>-1</sup>. The different amounts of carbon are controlled by only adjusting the content of acrylamide, in which the samples with doping acrylamide of 4.450, 7.000, and 12.000 g are denoted as Sn/SnO<sub>2</sub>@NC-1, Sn/SnO<sub>2</sub>@NC-2, and Sn/SnO<sub>2</sub>@NC-3, respectively. We have also designed and prepared the hydrogel-derived carbon and Sn/SnO<sub>2</sub> as control groups with the same conditions. All of the chemicals with analytical degrees are purchased from Shanghai Aladdin Biochemical Technology Co., Ltd. and used without further purification.

### Property characterization

The morphology and element distribution of the as-prepared samples are determined by field emission-scanning electron microscope (FE-SEM, TESCAN) and energy-dispersive spectrometer (EDS, BRUKER), respectively. The crystallographic structure of the samples is analyzed by X-ray diffraction (XRD) with CuK $\alpha$  radiation from 10 to 90° at a

step size of  $0.05^\circ$ . The valence state of the elements and Raman spectra of the sample are measured by X-ray photoelectron spectroscopy (XPS) and Renishaw Virsa Raman spectrometer, respectively. The different carbon contents of the composite powders are determined by thermogravimetric (TGA) under the air atmosphere in the temperature range of 30–1000 °C at a heating rate of  $10\text{ }^\circ\text{C min}^{-1}$ .

## Electrochemical performance

The electrochemical performance of those products is evaluated using CR2025-type coin cells. The working electrodes are carefully fabricated as follows. First, active material, poly (vinyl difluoride), and carbon black powders with a weight ratio of 8:1:1 are distributed in N-methyl pyrrolidone to prepare a slurry, and then, the slurry is coated on a Cu foil before being dried at 120 °C overnight, in which the loading mass of active material is kept at around  $0.8\text{ g cm}^{-2}$ . The working electrodes are assembled into the cells with 1 mol  $\text{L}^{-1}$  of  $\text{LiPF}_6$  in EC/DMC/DEC (1:1:1, in volume, provided from Guangdong Zhuguang New Energy Technology Co., Ltd.) as liquid electrolytes and lithium metal tablet as the counter electrodes in an Ar-filled glove box. The galvanostatic charge–discharge tests are measured using a Neware CT-3008A system (Shenzhen Neware Co., Ltd.) within a potential range of 0.01 to 3.00 V, and the cyclic voltammetry (CV) curves of the electrodes are monitored on a CHI660E electrochemistry workstation (Shanghai Chenhua Co., Ltd.) in the range of 0.01 to 3.00 V at a scan rate of  $0.10\text{ mV s}^{-1}$ , and the electrochemical impedance spectroscopy (EIS) curves are also recorded on the same electrochemistry workstation at a frequency range of  $10^{-5}$  to  $10^{-2}$  Hz with a voltage amplitude of 5.00 mV.

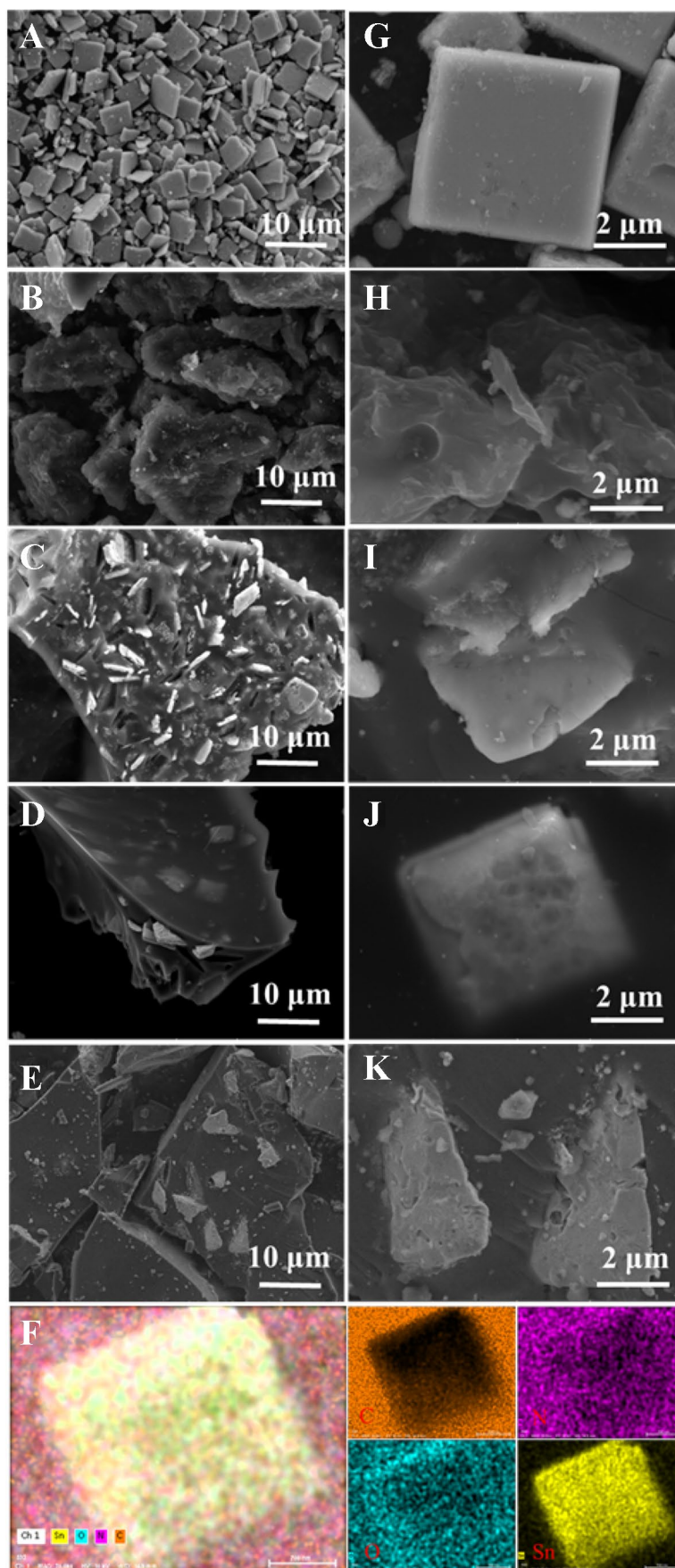
## Results and discussion

The SEM images of the SnO precursor, hydrogel derived carbon,  $\text{Sn/SnO}_2\text{@NC-1}$ ,  $\text{Sn/SnO}_2\text{@NC-2}$ , and  $\text{Sn/SnO}_2\text{@NC-3}$  powders and EDS mapping images of the  $\text{Sn/SnO}_2\text{@NC-2}$  powders are demonstrated in Fig. 1. As revealed in Fig. 1A, the SnO precursor presents a tight block-like structure and the particles maintain intact without severe agglomeration. It can be clearly revealed in Fig. 1G that the tetragonal SnO surface is very smooth with an average particle size of 5  $\mu\text{m}$ . The SEM images of the NC layer derived from the hydrogel are depicted in Fig. 1B, H, and it can be observed that the overall structure presents massive and porous, which can provide sufficient spaces to relieve the stress caused by volume changes, thus perfecting the cycling performance. As depicted in Fig. 1C–E, the typical structures of  $\text{Sn/SnO}_2\text{@NC-1}$ ,  $\text{Sn/SnO}_2\text{@NC-2}$ , and  $\text{Sn/SnO}_2\text{@NC-3}$  are gradually coated with the NC layer, which are obtained from

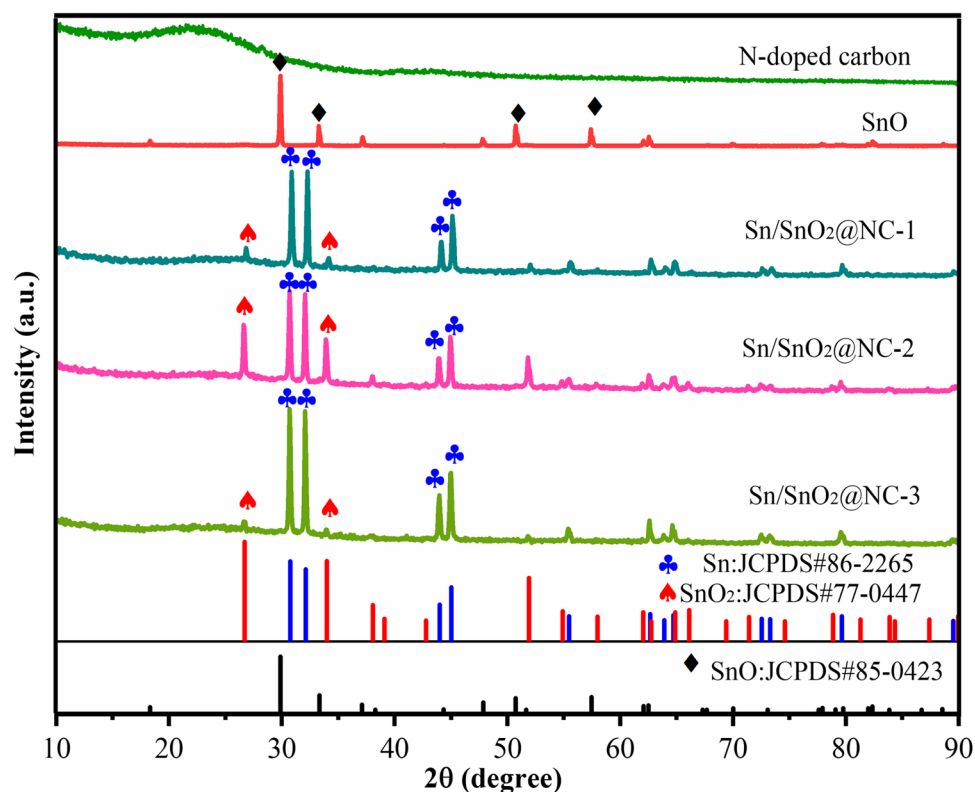
precisely controlling the added amounts of acrylamide. The corresponding block-like structures are further illustrated in Fig. 1I–K, in which the thickness change of the layer can be more clearly distinguished. Specifically, along with the increase of the carbon content, the NC layer on the surface of  $\text{Sn/SnO}_2$  stepwise thickens and merges into a solid mass. It can be obtained from Fig. 1C that the block-like particles on the surface of  $\text{Sn/SnO}_2\text{@NC-1}$  are densely congested in the carbon block and exhibit as unshaped agglomerations, in which most of the blocks agglomerate on the outside of the carbon block. On the contrary, the active blocks of  $\text{Sn/SnO}_2\text{@NC-3}$  are mostly surrounded by a thick NC wall, as shown in Fig. 1E, K. It is noteworthy that  $\text{Sn/SnO}_2\text{@NC-2}$  presents homogeneous distribution of small block-like particles when the addition of acrylamide is 7.000 g demonstrated in Fig. 1D, J, revealing that those uniform-sized particles are uniformly dispersed into the NC matrix and a thin layer of NC coating is encapsulated on the surface of the  $\text{Sn/SnO}_2\text{@NC-2}$  composite powders. Besides, the stable framework stemmed from the NC layer can accommodate the stress originated from volume changes of the Sn and  $\text{SnO}_2$  particles and therefore provide electronic and continuous paths for the  $\text{Sn/SnO}_2\text{@NC-2}$  composite powders. Those results are further confirmed by EDS elemental mapping images of the  $\text{Sn/SnO}_2\text{@NC-2}$  composite powders demonstrated in Fig. 1F, in which C, N, O, and Sn elements are homogeneously distributed throughout the whole tested area. N-doped carbon materials can improve the electrochemical performance of LIBs by generating more active sites and promoting the electronic conductivity. Therefore, there are reasons to believe that the  $\text{Sn/SnO}_2\text{@NC-2}$  composite materials can possess enhanced electrochemical properties, which will be further demonstrated in the following tests.

Figure 2 illustrates the XRD patterns of the SnO precursor,  $\text{Sn/SnO}_2\text{@NC-1}$ ,  $\text{Sn/SnO}_2\text{@NC-2}$ ,  $\text{Sn/SnO}_2\text{@NC-3}$ , and hydrogel-derived carbon powders. The lattice parameters of the SnO precursor are calculated as  $a=3.799$  and  $c=4.832$  according to the data of the (110) and (002) crystal planes, which are well indexed to the lattice constants of  $a=b=3.802$ ,  $c=4.836$ , and  $\alpha=\beta=\gamma=90^\circ$  (JCPDS#85–0423) of the tetragonal rutile structural SnO phase. The broad diffraction peak observed at around  $22.8^\circ$  can be ascribed to the (120) crystal plane of the graphite carbon phase (JCPDS#81–2220) originated from the hydrogel derived carbon. After being annealed at 400 °C for 2 h in a flowing  $\text{N}_2$  atmosphere, the  $\text{Sn/SnO}_2\text{@NC}$  composite powders exhibiting two characteristic diffraction peaks are well indexed to the typical tetragonal Sn (JCPDS#86–2265) and  $\text{SnO}_2$  phase (JCPDS#77–0447), in which the principal peaks at approximately  $30.6$ ,  $32.0$ ,  $43.9$ , and  $44.9^\circ$  are related to the (200), (101), (220), and (211) of Sn, and the weak intensity peaks at  $26.7$  and  $33.9^\circ$  are related to the (110) and (101) crystal planes of  $\text{SnO}_2$ , respectively. The formation of Sn/

**Fig. 1** SEM images of the SnO precursor (A, G), hydrogel derived carbon (B, H), Sn/SnO<sub>2</sub>@NC-1 (C, I), Sn/SnO<sub>2</sub>@NC-2 (D, J), Sn/SnO<sub>2</sub>@NC-3 (E, K) powders, and EDS mapping images (F) of the Sn/SnO<sub>2</sub>@NC-2 powders



**Fig. 2** XRD curves of the SnO precursor, Sn/SnO<sub>2</sub>@NC-1, Sn/SnO<sub>2</sub>@NC-2, Sn/SnO<sub>2</sub>@NC-3, and hydrogel derived carbon powders



SnO<sub>2</sub>@NC is due to the fact that SnO is firstly converted to metal Sn and SnO<sub>2</sub> and then, part of SnO<sub>2</sub> is partially reduced to Sn by hydrogel-derived carbon at high temperature during the calcination process, in which the weaker diffraction peaks are related to the Sn/SnO<sub>2</sub> particles wrapped in the NC matrix. Moreover, no other peaks are detected except Sn and SnO<sub>2</sub>, manifesting that the composite powders are successfully prepared without no impurity.

In order to further identify the chemical composition and valence state of the Sn/SnO<sub>2</sub>@NC-2 composite powders, high-resolution XPS tests are carried out and the corresponding curves are demonstrated in Fig. 3. It can be clearly discovered from Fig. 3A that the Sn/SnO<sub>2</sub>@NC-2 composite are composed of O, N, Sn, and C elements, which well matches with the EDS results. In the high-resolution XPS spectra of N 1s illustrated in Fig. 3B, three peaks located at 400.4 eV, 398.4, and 398.9 eV are ascribed to graphite N, pyridine N, and pyrrole N, respectively. The results further consolidate various types of N are successfully doped and uniformly distributed into the carbon matrix. As shown in Fig. 3C, the peaks located at 84.6, 285.1, and 286.5 eV can be assigned to C–C, C–O, and C=O, respectively. The Sn 3d XPS spectra collected from the Sn/SnO<sub>2</sub>@NC-2 composite are presented in Fig. 3D, in which two dominant peaks at 485.0 and 487.0 eV are assigned to Sn<sup>0</sup> and Sn<sup>4+</sup>, respectively. The peaks at about 493.4 and 495.4 are associated with Sn 3d<sub>5/2</sub> and Sn 3d<sub>3/2</sub>, respectively, with an interval of

the energy level splitting peaks about 8.4 eV, which further confirms the existence of Sn and SnO<sub>2</sub> in the Sn/SnO<sub>2</sub>@NC-2 composite and matches with the XRD results. In Fig. 3E, the high-resolution Sn 3d spectra of the pure SnO powders at 486.8 and 495.2 eV are corresponding to Sn<sup>2+</sup>. In addition, it can be clearly observed from Fig. 3F that two peaks observed on the surface of Sn/SnO<sub>2</sub> appearing at the binding energies of 485.0 and 487.0 eV are ascribed to the Sn<sup>0</sup> and Sn<sup>4+</sup> states, and the peaks situated at 493.4 and 495.4 eV are attributed to the Sn 3d<sub>5/2</sub> and Sn 3d<sub>3/2</sub>, respectively. Excitingly, the peak intensity of SnO in Sn/SnO<sub>2</sub>@NC-2 is higher than that in Sn/SnO<sub>2</sub>, which indicates that SnO microcubes are successfully transformed into the metal Sn and cassiterite SnO<sub>2</sub> phase. Those results are commendably consistent with the EDS analysis results to consolidate the fact that the Sn/SnO<sub>2</sub>@NC-2 composite powders are successful prepared, in which the incorporation of N atoms can improve electronic conductivity; there are reasons to believe that the Sn/SnO<sub>2</sub>@NC-2 composite powders may show elevated electrochemical properties.

Figure 4 presents the Raman spectra of Sn/SnO<sub>2</sub>@NC-1, Sn/SnO<sub>2</sub>@NC-2, Sn/SnO<sub>2</sub>@NC-3, and hydrogel derived carbon. It can be clearly observed from Fig. 4 that two obvious peaks at around 1350 and 1590 cm<sup>-1</sup> can be denoted as D band originated from the disordered or N doping carbon and the G band derived from the graphitic sp<sup>2</sup> hybrid ordered carbon, respectively. The degree of defects in the

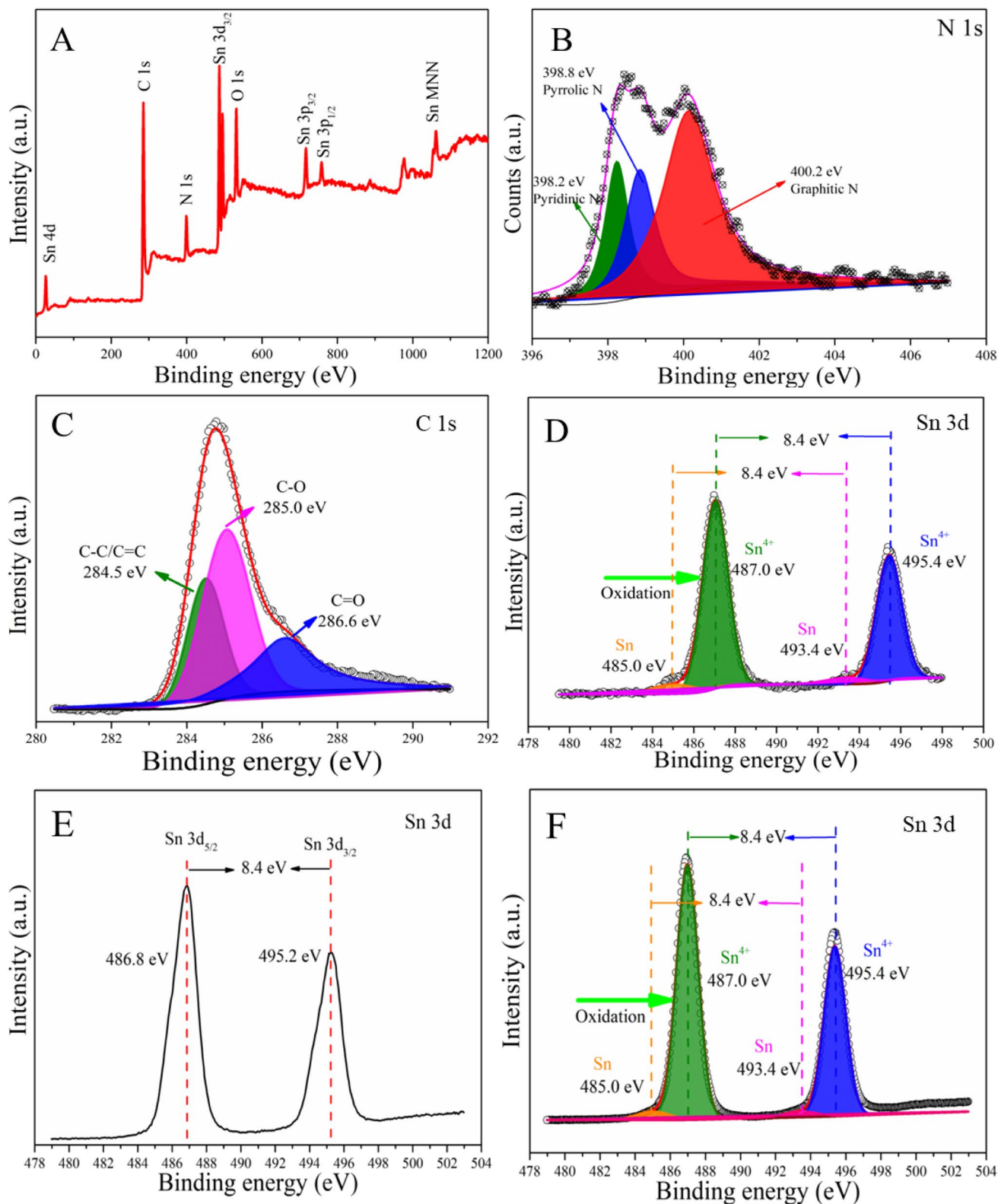


**Fig. 3** XPS spectra (A) of the Sn/SnO<sub>2</sub>@NC-2 samples, high resolution XPS spectra of N 1s (B), C 1s (C), and high-resolution XPS spectra of Sn 3d of Sn/SnO<sub>2</sub>@NC-2 (D), SnO (E), and Sn/SnO<sub>2</sub> (F), respectively

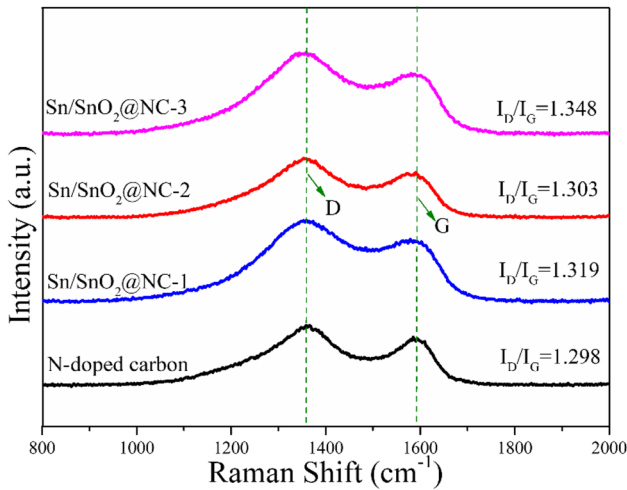
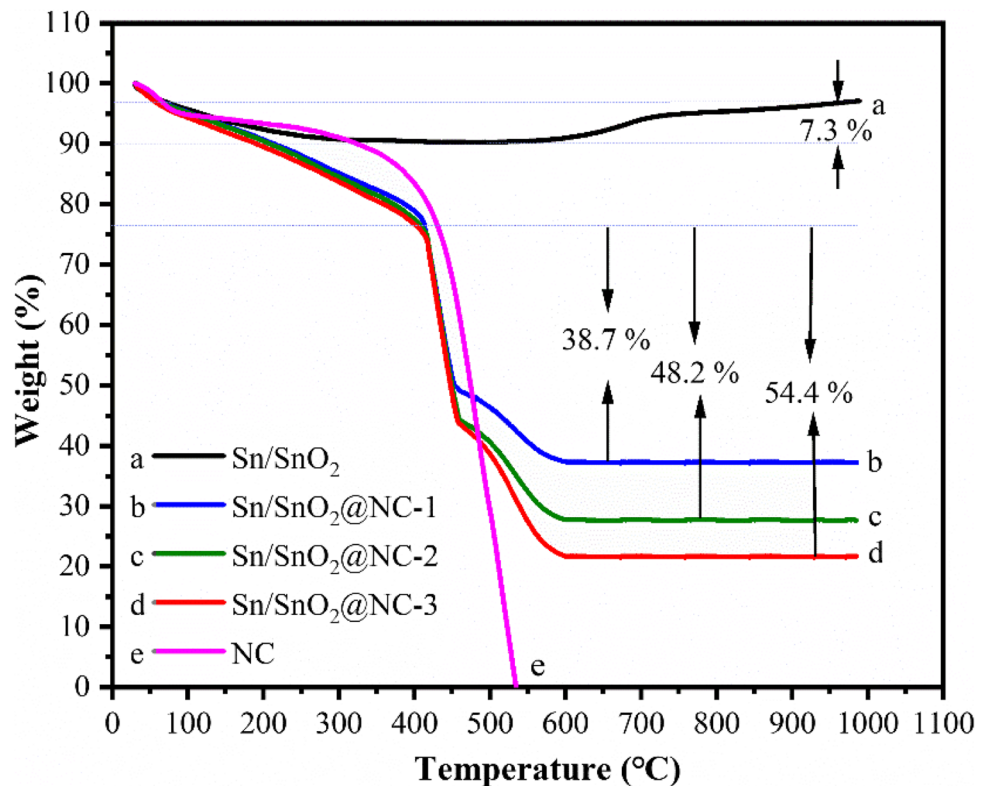


**Fig. 4** Raman spectra of Sn/SnO<sub>2</sub>@NC-1, Sn/SnO<sub>2</sub>@NC-2, Sn/SnO<sub>2</sub>@NC-3, and hydrogel-derived carbon

carbon-based materials can be usually evaluated by the peak intensity ratio of  $I_D/I_G$ . It can be found that the  $I_D/I_G$  is inclined to increase when the Sn/SnO<sub>2</sub> powders are individually encapsulated into the conductive NC matrix, in which the  $I_D/I_G$  values of Sn/SnO<sub>2</sub>@NC-1 (1.319), Sn/SnO<sub>2</sub>@NC-2 (1.303), and Sn/SnO<sub>2</sub>@NC-3 (1.348) are significantly higher than that of the hydrogel-derived carbon (1.298) due to the fact that the Sn/SnO<sub>2</sub> can provide more free electrons for the conduction to improve the conductivity of the material.

**Fig. 5** TG curves of Sn/SnO<sub>2</sub>, Sn/SnO<sub>2</sub>@NC-1, Sn/SnO<sub>2</sub>@NC-2, Sn/SnO<sub>2</sub>@NC-3, and hydrogel derived carbon



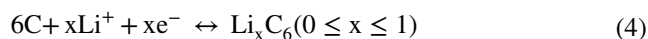
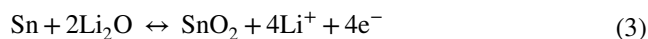
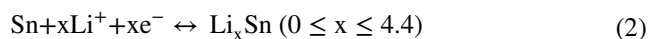
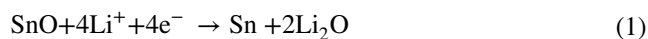
However, when less acrylamide is added, the proportion of Sn/SnO<sub>2</sub> increases. Although the defect sites increase correspondingly, the overall skeleton structure of the carbon material tends to collapse, leading to the degradation of the battery performance of the material. Hence, providential defects can not only increase the contact areas between the electrolytes and the electrodes by shortening the ion/electron diffusion distance, but also substantially improve electronic conductivity, which can be beneficial to the improvement of the electrochemical performance of LIBs.

Thermogravimetric (TG) analysis is an unambiguous measure to evaluate the carbon content in the Sn/SnO<sub>2</sub>, Sn/SnO<sub>2</sub>@NC-1, Sn/SnO<sub>2</sub>@NC-2, Sn/SnO<sub>2</sub>@NC-3, and hydrogel-derived carbon materials, and the corresponding curves are depicted in Fig. 5. It can be found from Fig. 5 that NC presents no residue when the temperature reaches 545 °C, which corresponds to the complete pyrolysis of NC, while the curves of Sn/SnO<sub>2</sub> exhibit an upward trend, which can be ascribed to the oxidation of the metal Sn. In addition, there are three weight loss stages in all of three curves of the Sn/SnO<sub>2</sub>@NC composite powders. First, the slight weight loss from 30 to 350 °C can be attributed to the evaporation of the adsorbed water on the surface of the composite materials. And then, between 350 and 450 °C, the marked weight decline can be caused by the oxidation of carbon according to the reaction of  $C + O_2 \rightarrow CO_2$ . Importantly, the weight loss of those composite powders exhibits a slow decline at approximately 500 °C due to the oxidation of Sn

to  $\text{SnO}_2$  according to the reaction of  $\text{Sn} + \text{O}_2 \rightarrow \text{SnO}_2$ . It can be obviously detected from the curves represented in Fig. 5 that three different weight loss degrees remain at 37.38, 27.88, and 21.67% at 600 °C, and the content of carbon in the  $\text{Sn}/\text{SnO}_2@\text{NC-1}$ ,  $\text{Sn}/\text{SnO}_2@\text{NC-2}$ , and  $\text{Sn}/\text{SnO}_2@\text{NC-3}$  composite powders is further calculated to be 46.63, 56.13, and 62.34%, respectively. Therefore, the theoretical specific capacity of the  $\text{Sn}/\text{SnO}_2@\text{NC-1}$ ,  $\text{Sn}/\text{SnO}_2@\text{NC-2}$ , and  $\text{Sn}/\text{SnO}_2@\text{NC-3}$  composite electrodes is calculated as 608.15, 569.39, and 544.05  $\text{mAh g}^{-1}$ , which can provide some theoretical references for the subsequent electrochemical performance.

The electrochemical performance of the  $\text{SnO}$ ,  $\text{Sn}/\text{SnO}_2@\text{NC-1}$ ,  $\text{Sn}/\text{SnO}_2@\text{NC-2}$ ,  $\text{Sn}/\text{SnO}_2@\text{NC-3}$ , and hydrogel-derived carbon electrodes for the LIBs are studied via galvanostatic charge–discharge tests at 100  $\text{mA g}^{-1}$  at 0.01–3.00 V. Figure 6A displays the voltage vs. charge–discharge specific capacity curves at the initial cycle, in which the  $\text{Sn}/\text{SnO}_2@\text{NC-2}$  electrode delivers discharge specific capacity of 1132  $\text{mAh g}^{-1}$  with an initial coulombic efficiency (ICE) of 71.0% in the first cycle, while the pure  $\text{SnO}$ , hydrogel-derived carbon,  $\text{Sn}/\text{SnO}_2@\text{NC-1}$ , and  $\text{Sn}/\text{SnO}_2@\text{NC-3}$  electrodes reveal ICE of 40.07, 40.25, 55.29, and 60.26%, respectively. The improved ICE of the  $\text{Sn}/\text{SnO}_2@\text{NC-2}$  electrode is attributed to the fact that hydrogel perfectly encapsulates the block-like  $\text{Sn}/\text{SnO}_2$  composite powders and protects them from direct contact with the electrolytes, hence reducing the side reactions on the electrode/electrolyte interface. Figure 6B exhibits initial three CV curves of the  $\text{Sn}/\text{SnO}_2@\text{NC-2}$  electrode within a voltage scope of 0.01–3.00 V at a scan rate of 0.1  $\text{mV s}^{-1}$ . Upon the first cathodic scan, the reduction peaks below 0.95 V are correlated with the emergence of the unstable solid-electrolyte interface (SEI) and some irreversible reactions, accompanying with the conversion from  $\text{SnO}_2$  to  $\text{LiO}_2$  and  $\text{Sn}$  corresponding to Eq. (1). It can be distinctly detected that the peak at 0.34 V and a small peak at around 0.57 V can be explained as the formation of  $\text{Li}_x\text{Sn}$  ( $0 \leq x \leq 4.4$ ) with the multistep alloying reactions described in Eq. (2). Afterwards, a sharp reaction peak appearing at 0.13 V denotes the fact that lithium ions successfully insert into the carbon layer

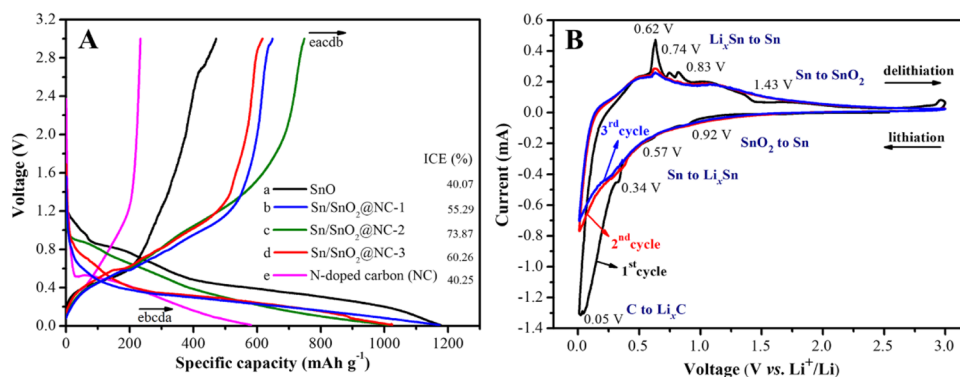
to form  $\text{Li}_x\text{C}_6$  ( $0 \leq x \leq 1$ ) according to Eq. (4). Turning to the first anodic scan, a series of peaks at about 0.62, 0.74, and 0.83 V are assigned to the stepwise oxidations from  $\text{Li}_x\text{Sn}$  to  $\text{Sn}$ , respectively. Subsequently, the disappearing cathodic peak of  $\text{Sn}/\text{SnO}_2@\text{NC-2}$  at 1.43 V in the following cycles can be ascribed to the irreversible reaction from  $\text{Sn}$  and  $\text{Li}_2\text{O}$  to  $\text{SnO}_2$  according to Eq. (3), indicating the decreasing capacity with lower coulombic efficiency. Furthermore, the plots of the  $\text{Sn}/\text{SnO}_2@\text{NC-2}$  electrode nearly overlapping in the subsequent cycles are manifested as an unchanged peak current intensity, indicating that a firm SEI film formed on the NC surface during the first cycle can prevent the direct contact between active materials and liquid electrolytes to maintain an intact structure during the subsequent cycles, thereby leading to the excellent reversibility of the  $\text{Sn}/\text{SnO}_2@\text{NC-2}$  electrode. The initial irreversible capacity of the  $\text{Sn}/\text{SnO}_2@\text{NC-2}$  electrode can be associated with the inevitable formation of the SEI film and decomposition of electrolytes, which are consistent with the above galvanostatic charge–discharge results. The results suggest that the conductive NC coating is sufficient to inhibit the serious volume expansion of  $\text{Sn}$  and  $\text{SnO}_2$  during the alloying/dealloying process, and the heterostructure can effectively strengthen the reversibility of conversion and alloying process.



$$Z' = R_s + R_{ct} + \sigma\omega^{-0.5} \quad (5)$$

$$D_{\text{Li}^+} = \frac{R^2 T^2}{2A^2 n^4 F^2 C^2 \sigma^2} \quad (6)$$

**Fig. 6** Initial galvanostatic charge–discharge curves (A) of the coin cells assembled with the  $\text{SnO}$ ,  $\text{Sn}/\text{SnO}_2@\text{NC-1}$ ,  $\text{Sn}/\text{SnO}_2@\text{NC-2}$ ,  $\text{Sn}/\text{SnO}_2@\text{NC-3}$ , and hydrogel-derived carbon electrodes at 100  $\text{mA g}^{-1}$  and CV curves (B) of the cells assembled with the  $\text{Sn}/\text{SnO}_2@\text{NC-2}$  electrode





The cycling profiles of the SnO, Sn/SnO<sub>2</sub>@NC-1, Sn/SnO<sub>2</sub>@NC-2, Sn/SnO<sub>2</sub>@NC-3, and hydrogel derived carbon electrodes at 100 mA g<sup>-1</sup> for 100 cycles are displayed in Fig. 7A. It is obviously observed from the curves that the capacity of the pure SnO electrode quickly degrades and reaches nearly close to zero after 5 cycles, while the NC electrode presents superior rate capability for the test. Compared with the SnO and NC electrodes, the Sn/SnO<sub>2</sub>@NC composite electrodes exhibit preferable cycling performance, in which the Sn/SnO<sub>2</sub>@NC-2 electrode delivers high reversible specific capacity of 471.4 mAh g<sup>-1</sup> after 100 cycles at 100 mA g<sup>-1</sup> that can be ascribed to a strong electronic coupling between NC and Sn/SnO<sub>2</sub>. In contrast, the Sn/SnO<sub>2</sub>@NC-1 and Sn/SnO<sub>2</sub>@NC-3 composite electrodes deliver lower capacities of 330.3 and 202.4 mAh g<sup>-1</sup> after 100 cycles, respectively. Therefore, the increasing reversible capacity of the Sn/SnO<sub>2</sub>@NC-2 electrode can be originated from the

nitrogen-doped heterostructure, which can not only provide additional active sites for lithium ions, but also enable the rapid migration of lithium ions to improve the lithium storage performance. To further explore the superiority of the Sn/SnO<sub>2</sub>@NC-2 electrode, the rate capability of the SnO, Sn/SnO<sub>2</sub>@NC-1, Sn/SnO<sub>2</sub>@NC-2, Sn/SnO<sub>2</sub>@NC-3, and NC electrodes is also recorded at step-increased current density and the corresponding results are illustrated in Fig. 7B. It is clearly observed that the average reversible specific capacity of the NC electrode is inferior compared with that of the Sn/SnO<sub>2</sub>@NC electrodes, in which the value is only 237.8, 216.7, 170.7, 129.9, and 97.3 mAh g<sup>-1</sup> at 100, 200, 300, 500, and 1000 mA g<sup>-1</sup>, respectively. In contrast, it can be easily observed that the Sn/SnO<sub>2</sub>@NC-2 composite electrode displays the significantly improved rate capability with the average discharge reversible capacity of 561.5, 469.7, 392.6, 315.1, and 190.3 at the same rates, respectively. Moreover,

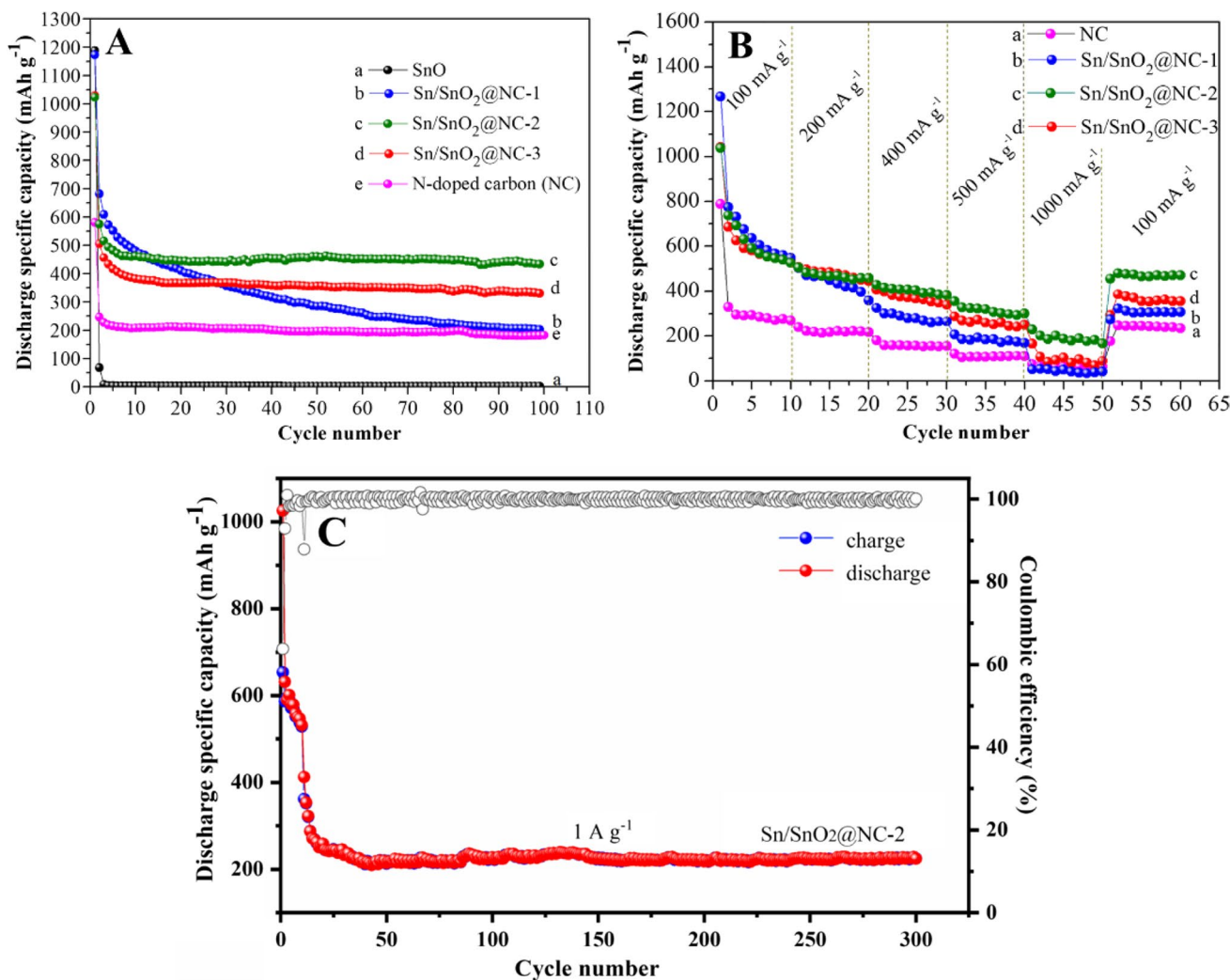


**Fig. 7** Cycle performance (A) of the coin cells with the SnO, Sn/SnO<sub>2</sub>@NC-1, Sn/SnO<sub>2</sub>@NC-2, Sn/SnO<sub>2</sub>@NC-3, and hydrogel-derived carbon electrodes at 100 mA g<sup>-1</sup> for 100 cycles, rate capability (B), and long cycling performance (C) of Sn/SnO<sub>2</sub>@NC-2 at 1 A g<sup>-1</sup> for 300 cycles

the reversible discharge specific capacity of the Sn/SnO<sub>2</sub>@NC-2 electrode can be maintained at 441.1 mAh g<sup>-1</sup> when the current density is adjusted to 100 mA/g, which is largely attributed to the stable structure resulting from the perfect NC coating on the surface of the composite electrode. The long cycling performance of Sn/SnO<sub>2</sub>@NC-2 at 1 A g<sup>-1</sup> for 300 cycles is also demonstrated in Fig. 7C, in which the electrode is first cycled at 0.1 A g<sup>-1</sup> for 10 cycles and then cycled at 1 A g<sup>-1</sup> for the rest. The discharge specific capacity can be still maintained at 224.4 mAh g<sup>-1</sup> after 300 cycles, indicating the preferable electrochemical stability of the Sn/SnO<sub>2</sub>@NC-2 electrode. The good rate capability at high current densities can be attributed to the conductive NC matrix, which can alleviate the serious volume changes of Sn and SnO<sub>2</sub> during the cycling processes.

Electrochemical impedance spectroscopy (EIS) is employed to investigate the reaction kinetics of the SnO, Sn/SnO<sub>2</sub>@NC-1, Sn/SnO<sub>2</sub>@NC-2, Sn/SnO<sub>2</sub>@NC-3, and hydrogel-derived carbon electrodes for the fresh coin cells, and the corresponding curves are shown in Fig. 8. The EIS diagrams can be well fitted by the equivalent circuit described as  $[R_s(R_{ct}/CPE)W_0]$  and the detailed fitting values of the parameters are listed in Table 1. All of the Nyquist plots are composed of a semicircle located at high-frequency region and a sloping line in the low-frequency region, in which the diameter of the semicircle and the slope of the line stand for the charge transfer impedance ( $R_{ct}$ ) between electrolyte and electrode materials and Warburg impedance ( $Z_w$ ), respectively. It can be clearly found from Fig. 8A that the Sn/SnO<sub>2</sub>@NC samples reveal a smaller semicircle diameter and  $R_{ct}$  value than that of the SnO electrode due to the enhanced electronic conductivity in the presence of the NC layer, in which the  $R_{ct}$  value of Sn/SnO<sub>2</sub>@NC-2 is 176.6 Ω, while the values of SnO, Sn/SnO<sub>2</sub>@NC-1, Sn/SnO<sub>2</sub>@NC-3, and NC are 416.9, 221.7, 204.1, and 150.3 Ω, respectively. The results further support the superior rate performance of Sn/SnO<sub>2</sub>@NC-2 due to the fact that the hydrogel-derived NC layer can accelerate the transfer of lithium ions, therefore reducing the side reactions and lowering the charge-transfer resistances. Furthermore, the Warburg coefficient and

**Table 1** Fitted values of the corresponding parameters of the as-prepared electrodes

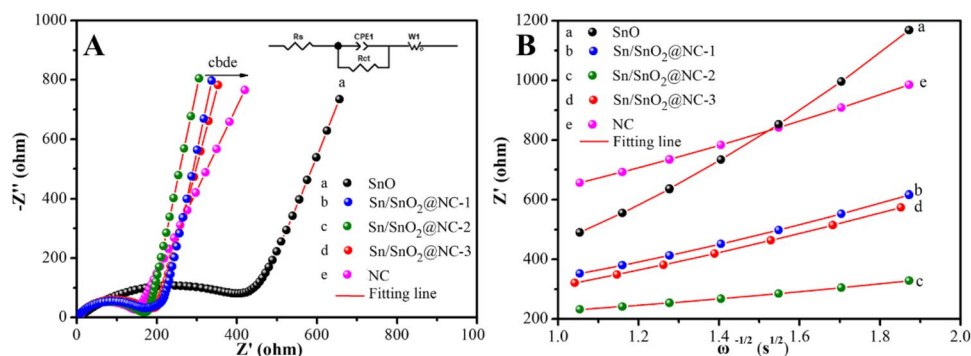
Type	$R_{ct}$ (Ω)	$\sigma$ (Ω cm <sup>2</sup> s <sup>-1/2</sup> )	$D_{Li^+}$ (cm <sup>2</sup> s <sup>-1</sup> )
SnO	416.9	825.4	$7.501 \times 10^{-17}$
Sn/SnO <sub>2</sub> @NC-1	221.7	312.0	$5.249 \times 10^{-16}$
Sn/SnO <sub>2</sub> @NC-2	176.6	117.6	$3.695 \times 10^{-15}$
Sn/SnO <sub>2</sub> @NC-3	204.1	322.0	$4.928 \times 10^{-16}$
NC	150.3	401.3	$3.173 \times 10^{-16}$

diffusion coefficient of lithium ions ( $D_{Li^+}$ ) of the samples can be calculated according to the following Eqs. (5, 6). It can be obviously found from Table 1 that the Sn/SnO<sub>2</sub>@NC-2 electrode possesses the minimum  $\sigma$  value of 117.6 Ω cm<sup>2</sup> s<sup>-1/2</sup> and preferable  $D_{Li^+}$  value of  $3.695 \times 10^{-15}$  cm<sup>2</sup> s<sup>-1</sup> compared with other electrodes, which further consolidates the fact that the NC coating with a stable framework can not only effectively enhance the electronic conductivity but also facilitate Li<sup>+</sup> transport and diffusion kinetics of the Sn/SnO<sub>2</sub>@NC-2 electrode.

## Conclusions

The Sn/SnO<sub>2</sub>@NC composite materials are successfully fabricated from SnO through facile hydrothermal, sol-gel, and carbonization processes, in which the as-prepared Sn/SnO<sub>2</sub>@NC-2 composite powders demonstrate uniform Sn/SnO<sub>2</sub> microcubes encapsulated inside the NC layer when the addition of acrylamide increases to 7.000 g. The NC coating can provide more active sites for electrochemical reactions and ensure better transport kinetics during the charging and discharging process. Moreover, the Sn/SnO<sub>2</sub>@NC-2 electrode exhibits decent rate capability and superior cycling capability when employed as anode electrodes in LIBs, which can be ascribed to the fact that the NC coating can not only alleviate the volume changes, but also enhance the electronic conductivity of the electrodes during the alloying and dealloying process. Therefore, the Sn/SnO<sub>2</sub>@

**Fig. 8** Nyquist and the corresponding fitting plots (A), and the fitted curves (B) of  $Z'$  vs.  $\omega^{-1/2}$  at the low-frequency range of the coin cells assembled with the SnO, Sn/SnO<sub>2</sub>@NC-1, Sn/SnO<sub>2</sub>@NC-2, Sn/SnO<sub>2</sub>@NC-3, and hydrogel-derived carbon electrodes



NC-2 electrode can be a promising anode material for high-performance LIBs.

**Funding** This work was financially supported by the National Natural Science Foundation of China (No. 51874046), the Outstanding Youth Foundation of Hubei Province (No. 2020CFA090), and the Hunan Provincial Natural Science Foundation of China (No. 2021JJ50138).

## References

- Ding S, Cheng W, Zhang L, Du G, Hao X, Nie G, Xu B, Zhang M, Su Q, Serra CA (2021) Organic molecule confinement reaction for preparation of the Sn nanoparticles@graphene anode materials in Lithium-ion battery. *J Colloid Interface Sci* 589:308–317. <https://doi.org/10.1016/j.jcis.2020.12.086>
- Ardhi REA, Liu G, Tran MX, Hudaya C, Kim JY, Yu H, Lee JK (2018) Self-relaxant superelastic matrix derived from C<sub>60</sub> Incorporated Sn nanoparticles for ultra-high-performance Li-ion batteries. *ACS Nano* 12(6):5588–5604. <https://doi.org/10.1021/acsnano.8b01345>
- Wang J, Nie Y, Miao C, Tan Y, Wen M, Xiao W (2021) Enhanced electrochemical properties of Ni-rich layered cathode materials via Mg<sup>2+</sup> and Ti<sup>4+</sup> co-doping for lithium-ion batteries. *J Colloid Interface Sci* 601:853–862. <https://doi.org/10.1016/j.jcis.2021.05.167>
- Song D, Park J, Kim K, Lee LS, Seo JY, Oh Y-K, Kim Y-J, Ryou M-H, Lee YM, Lee K (2017) Recycling oil-extracted microalgal biomass residues into nano/micro hierarchical Sn/C composite anode materials for lithium-ion batteries. *Electrochim Acta* 250:59–67. <https://doi.org/10.1016/j.electacta.2017.08.045>
- Mou H, Chen S, Xiao W, Miao C, Li R, Xu G, Xin Y, Nie S (2021) Encapsulating homogenous ultra-fine SnO<sub>2</sub>/TiO<sub>2</sub> particles into carbon nanofibers through electrospinning as high-performance anodes for lithium-ion batteries. *Ceram Int* 47(14):19945–19954. <https://doi.org/10.1016/j.ceramint.2021.03.329>
- Li R, Xiao W, Miao C, Fang R, Wang Z, Zhang M (2019) Sphere-like SnO<sub>2</sub>/TiO<sub>2</sub> composites as high-performance anodes for lithium ion batteries. *Ceram Int* 45(10):13530–13535. <https://doi.org/10.1016/j.ceramint.2019.04.059>
- Shao F, Li H, Yao L, Xu S, Li G, Li B, Zou C, Yang Z, Su Y, Hu N, Zhang Y (2021) Binder-free, flexible, and self-standing non-woven fabric anodes based on graphene/Si hybrid fibers for high-performance Li-ion batteries. *ACS Appl Mater Interfaces* 13(23):27270–27277. <https://doi.org/10.1021/acsnami.1c04277>
- Nie S, Liu L, Liu J, Xie J, Zhang Y, Xia J, Yan H, Yuan Y, Wang X (2018) Nitrogen-doped TiO<sub>2</sub>-C composite nanofibers with high-capacity and long-cycle life as anode materials for sodium-ion batteries. *Nanomicro Lett* 10(4):1–13. <https://doi.org/10.1007/s40820-018-0225-1>
- Nie Y, Xiao W, Miao C, Xu M, Wang C (2020) Effect of calcining oxygen pressure gradient on properties of LiNi<sub>0.8</sub>Co<sub>0.15</sub>Al<sub>0.05</sub>O<sub>2</sub> cathode materials for lithium ion batteries. *Electrochim Acta* 334:135654. <https://doi.org/10.1016/j.electacta.2020.135654>
- Wang J, Liu C, Xu G, Miao C, Wen M, Xu M, Wang C, Xiao W (2022) Strengthened the structural stability of in-situ F-doping Ni-rich LiNi<sub>0.8</sub>Co<sub>0.15</sub>Al<sub>0.05</sub>O<sub>2</sub> cathode materials for lithium-ion batteries. *Chem Eng J* 135537. <https://doi.org/10.1016/j.cej.2022.135537>
- Xiao W, Nie Y, Miao C, Wang J, Tan Y, Wen M (2021) Structural design of high-performance Ni-rich LiNi<sub>0.83</sub>Co<sub>0.11</sub>Mn<sub>0.06</sub>O<sub>2</sub> cathode materials enhanced by Mg<sup>2+</sup> doping and Li<sub>3</sub>PO<sub>4</sub> coating for lithium ion battery. *J Colloid Interface Sci* 607:1071–1082. <https://doi.org/10.1016/j.jcis.2021.09.067>
- Wang Z, Kou Z, Miao C, Xiao W (2019) Improved performance all-solid-state electrolytes with high compacted density of mono-dispersed spherical Li<sub>1.3</sub>Al<sub>0.3</sub>Ti<sub>1.7</sub>(PO<sub>4</sub>)<sub>3</sub> particles. *Ceram Int* 45(11):14469–14473. <https://doi.org/10.1016/j.ceramint.2019.04.192>
- Sui Y, Zhou J, Wang X, Wu L, Zhong S, Li Y (2021) Recent advances in black-phosphorus-based materials for electrochemical energy storage. *Mate Today* 42:117–136. <https://doi.org/10.1016/j.mattod.2020.09.005>
- Nie Y, Xiao W, Miao C, Fang R, Kou Z, Wang D, Xu M, Wang C (2020) Boosting the electrochemical performance of LiNi<sub>0.8</sub>Co<sub>0.15</sub>Al<sub>0.05</sub>O<sub>2</sub> cathode materials in-situ modified with Li<sub>1.3</sub>Al<sub>0.3</sub>Ti<sub>1.7</sub>(PO<sub>4</sub>)<sub>3</sub> fast ion conductor for lithium-ion batteries. *Electrochim Acta* 353:136477. <https://doi.org/10.1016/j.electacta.2020.136477>
- Kou Z-Y, Lu Y, Miao C, Li J-Q, Liu C-J, Xiao W (2021) High-performance sandwiched hybrid solid electrolytes by coating polymer layers for all-solid-state lithium-ion batteries. *Rare Met* 40(11):3175–3184. <https://doi.org/10.1007/s12598-020-01678-w>
- Feng Y, Bai C, Wu K, Dong H, Ke J, Huang X, Xiong D, He M (2020) Fluorine-doped porous SnO<sub>2</sub>@C nanosheets as a high performance anode material for lithium ion batteries. *J Alloy Compd* 843. <https://doi.org/10.1016/j.jallcom.2020.156085>
- Jiang Y, Jiang J, Wang Z, Han M, Liu X, Yi J, Zhao B, Sun X, Zhang J (2020) Li<sub>4.4</sub>Sn encapsulated in hollow graphene spheres for stable Li metal anodes without dendrite formation for long cycle-life of lithium batteries. *Nano Energy* 70. <https://doi.org/10.1016/j.nanoen.2020.104504>
- Xu Y, Yuan T, Bian Z, Yang J, Zheng S (2020) Tuning particle and phase formation of Sn/carbon nanofibers composite towards stable lithium-ion storage. *J Power Sources* 453. <https://doi.org/10.1016/j.jpowsour.2019.227467>
- Zhang W, Zheng M, Li F, You Y, Jiang D, Yuan H, Ma L, Shen W (2021) SnO<sub>x</sub>/graphene anode material with multiple oxidation states for high-performance Li-ion batteries. *Nanotechnology* 32(19):195407. <https://doi.org/10.1088/1361-6528/abe2c9>
- Mou H, Xin Y, Miao C, Nie S, Chen S, Xiao W (2021) Amorphous SnO<sub>2</sub> nanoparticles embedded into a three-dimensional porous carbon matrix as high-performance anodes for lithium-ion batteries. *Electrochim Acta* 397:139286. <https://doi.org/10.1016/j.electacta.2021.139286>
- Li X, He X, Xu Y, Huang L, Li J, Sun S, Zhao J (2015) Superiority of the bi-phasic mixture of a tin-based alloy nanocomposite as the anode for lithium ion batteries. *J Mater Chem A* 3(7):3794–3800. <https://doi.org/10.1039/c4ta06862a>
- Liang S, Zhu X, Lian P, Yang W, Wang H (2011) Superior cycle performance of Sn@C/graphene nanocomposite as an anode material for lithium-ion batteries. *J Solid State Chem* 184(6):1400–1404. <https://doi.org/10.1016/j.jssc.2011.03.052>
- Fu Z, Li X, Xu G (2014) Novel electrospun SnO<sub>2</sub>@carbon nanofibers as high performance anodes for lithium-ion batteries. *Cryst Res Technol* 49(7):441–445. <https://doi.org/10.1002/crat.201300211>
- Zhang F, Wang Y, Guo W, Mao P, Rao S, Xiao P (2020) Yolk-shelled Sn@C@MnO hierarchical hybrid nanospheres for high performance lithium-ion batteries. *J Alloy Compd* 829. <https://doi.org/10.1016/j.jallcom.2020.154579>
- Zhang L, Zhao K, Sun C, Yu R, Zhuang Z, Li J, Xu W, Wang C, Xu W, Mai L (2020) Compact Sn/SnO<sub>2</sub> microspheres with gradient composition for high volumetric lithium storage. *Energy Storage Mater* 25:376–381. <https://doi.org/10.1016/j.ensm.2019.10.003>
- Lee JH, Oh SH, Jeong SY, Kang YC, Cho JS (2018) Rattle-type porous Sn/C composite fibers with uniformly distributed

- nanovoids containing metallic Sn nanoparticles for high-performance anode materials in lithium-ion batteries. *Nanoscale* 10(45):21483–21491. <https://doi.org/10.1039/c8nr06075d>
27. Huang K, Xing Z, Wang L, Wu X, Zhao W, Qi X, Wang H, Ju Z (2018) Direct synthesis of 3D hierarchically porous carbon/Sn composites via in situ generated NaCl crystals as templates for potassium-ion batteries anode. *J Mater Chem A* 6(2):434–442. <https://doi.org/10.1039/c7ta08171e>
  28. Sivashanmugam A, Kumar TP, Renganathan NG, Gopukumar S, Wohlfahrt-Mehrens M, Garche J (2005) Electrochemical behavior of Sn/SnO<sub>2</sub> mixtures for use as anode in lithium rechargeable batteries. *J Power Sources* 144(1):197–203. <https://doi.org/10.1016/j.jpowsour.2004.12.047>
  29. Mousavi M, Abolhassani R, Hosseini M, Akbarnejad E, Mojallal MH, Ghasemi S, Mohajerzadeh S, Sanaee Z (2021) Antimony doped SnO<sub>2</sub> nanowire@C core-shell structure as a high-performance anode material for lithium-ion battery. *Nanotechnology* 32(28). <https://doi.org/10.1088/1361-6528/abf456>
  30. Agubra VA, Zuniga L, Flores D, Campos H, Villarreal J, Alcoutlabi M (2017) A comparative study on the performance of binary SnO<sub>2</sub>/NiO/C and Sn/C composite nanofibers as alternative anode materials for lithium ion batteries. *Electrochim Acta* 224:608–621. <https://doi.org/10.1016/j.electacta.2016.12.054>
  31. Gao S, Wang N, Li S, Li D, Cui Z, Yue G, Liu J, Zhao X, Jiang L, Zhao Y (2020) A multi-wall Sn/SnO<sub>2</sub>@carbon hollow nanofiber anode material for high-rate and long-life lithium-ion batteries. *Angew Chem Int Ed Engl* 59(6):2465–2472. <https://doi.org/10.1002/anie.201913170>
  32. Liu S, Pang F, Zhang Q, Guo R, Wang Z, Wang Y, Zhang W, Ou J (2018) Stable nanoporous Sn/SnO<sub>2</sub> composites for efficient electroreduction of CO<sub>2</sub> to formate over wide potential range. *Appl Mater Today* 13:135–143. <https://doi.org/10.1016/j.apmt.2018.08.014>
  33. Jiang W, Wang W, Liu L, Wang H, Xu Z, Li F, Fu H, Lv H, Chen L, Kang Y (2019) Sandwich-like Sn/SnO<sub>2</sub>@Graphene anode composite assembled by fortissimo penetration of  $\gamma$ -ray and interlamellar limitation of graphene oxide. *J Alloy Compd* 779:856–862. <https://doi.org/10.1016/j.jallcom.2018.11.296>
  34. Sun Q, Kong X, Liu W, Xu B, Hu P, Gao Z, Huang Y (2020) Flakes-stacked Sn/SnO<sub>2</sub>/C composite as highly stable anode material for lithium-ion batteries. *J Alloy Compd* 831. <https://doi.org/10.1016/j.jallcom.2020.154677>
  35. Li R, Nie S, Miao C, Xin Y, Mou H, Xu G, Xiao W (2022) Heterostructural Sn/SnO<sub>2</sub> microcube powders coated by a nitrogen-doped carbon layer as good-performance anode materials for lithium ion batteries. *J Colloid Interface Sci* 606:1042–1054. <https://doi.org/10.1016/j.jcis.2021.08.112>
  36. Uchiyama H, Nakanishi S, Kozuka H (2014) Hydrothermal synthesis of nanostructured SnO particles through crystal growth in the presence of gelatin. *J Solid State Chem* 217:87–91. <https://doi.org/10.1016/j.jssc.2014.05.023>
  37. Kim Y-J, Park M-S, Sohn H-J, Lee H (2011) Electrochemical behaviors of SnO and Sn anodes for lithium rechargeable batteries. *J Alloy Compd* 509(12):4367–4371. <https://doi.org/10.1016/j.jallcom.2011.01.061>
  38. Hassan FM, Chen Z, Yu A, Chen Z, Xiao X (2013) Sn/SnO<sub>2</sub> embedded in mesoporous carbon nanocomposites as negative electrode for lithium ion batteries. *Electrochim Acta* 87:844–852. <https://doi.org/10.1016/j.electacta.2012.09.015>
  39. Wen X, Xiang K, Zhu Y, Xiao L, Liao H, Chen W, Chen X, Chen H (2020) 3D hierarchical nitrogen-doped graphene/CNTs microspheres as a sulfur host for high-performance lithium-sulfur batteries. *J Alloy Compd* 815:152350. <https://doi.org/10.1016/j.jallcom.2019.152350>
  40. Wang G, Xu Y, Yue H, Jin R, Gao S (2020) NiMoS<sub>4</sub> nanocrystals anchored on N-doped carbon nanosheets as anode for high performance lithium ion batteries. *J Colloid Interface Sci* 561:854–860. <https://doi.org/10.1016/j.jcis.2019.11.068>
  41. Dong G, Fang Y, Liao S, Zhu K, Yan J, Ye K, Wang G, Cao D (2021) 3D tremella-like nitrogen-doped carbon encapsulated few-layer MoS<sub>2</sub> for lithium-ion batteries. *J Colloid Interface Sci* 601:594–603. <https://doi.org/10.1016/j.jcis.2021.05.150>

**Publisher's note** Springer Nature remains neutral with regard to jurisdictional claims in published maps and institutional affiliations.

Springer Nature or its licensor holds exclusive rights to this article under a publishing agreement with the author(s) or other rightsholder(s); author self-archiving of the accepted manuscript version of this article is solely governed by the terms of such publishing agreement and applicable law.